Classical, semiclassical, and quantum dynamics in the lithium Stark system

Michael Courtney, Neal Spellmeyer, Hong Jiao, and Daniel Kleppner

Department of Physics and Research Laboratory for Electronics, Massachusetts Institute of Technology,
77 Massachusetts Avenue, Cambridge, Massachusetts 02139

We report a study of the connections between classical dynamics and quantum structure based on the lithium Stark spectrum. The system undergoes a transition to chaos as the energy or field is increased. We employ scaled-energy spectroscopy and closed-orbit theory to relate the photoabsorption spectrum to classical orbits. Bifurcations of closed orbits provide a semiclassical interpretation of the spectrum as it evolves from a simple sinusoidal modulation at positive energy to a discrete spectrum below the classical ionization limit. The system is compared with the closely related, but completely regular, hydrogen Stark system. The differences between their spectra and the development of chaos in lithium can be understood in terms of scattering of recurrences from one closed orbit to another by the alkali-metal core.

PACS number(s): 32.60.+i, 05.45.+b, 03.65.Sq

I. INTRODUCTION

The behavior of atoms in electric fields has attracted attention since the earliest days of quantum mechanics. Numerous experimental and theoretical studies have elucidated quantum Stark structure [1, 2], but our understanding of the connections between quantum structure and classical dynamics, particularly in regimes of chaos, is far from complete. Hydrogen has occupied a prominent position in studies of Stark structure because its Hamiltonian is separable and analytic quantum and classical solutions are possible. A consequence of such separability is that the classical motion is always regular. In contrast, the dynamics of an alkali-metal atom in an applied field is inherently chaotic. Armed with recent advances for relating the spectra of chaotic systems to their classical dynamics, we have returned to the problem of the Stark spectrum of alkali-metal atoms in order to deepen our understanding of disorderly motion in the semiclassical regime—the problem of quantum chaos.

Two approaches for associating spectral features with classical dynamics in conservative systems are now well established. The first takes quantum structure as its starting point and classifies systems according to the fluctuations of their eigenvalues. The distribution of energies between adjacent levels for orderly classical systems is generally Poissonian, whereas for disorderly motion it generally resembles the distribution of eigenvalues of ensembles of random matrices [3]. This approach tends to emphasize small scale spectral correlations, though large scale correlations can also be measured.

The second approach takes classical trajectories as the starting point [4]. Closed-orbit theory asserts that every closed orbit—that is, every periodic trajectory that begins and ends at the nucleus—produces a sinusoidal modulation in the photoabsorption spectrum [5]. This approach makes it possible to compute spectra from a knowledge of the classical orbits. It is attractive for interpreting experiments because it emphasizes large scale spectral structures that are easily distinguishable in low-

resolution spectra. Such structures arise for short-period orbits that are relatively easy to compute. As the resolution is increased, longer- and longer-period orbits need to be considered. How far this process can be carried forward remains an open question, but to the extent that it can be carried out, it provides a bridge between classical and quantum mechanics.

These two approaches have been tested numerically in simple systems such as chaotic billiards and the Henon-Heiles potential [3, 4], but few chaotic quantum systems have been studied experimentally under conditions of close control. Prominent among such systems has been the diamagnetic hydrogen atom, which has proven to be an excellent testing ground for energy-level statistics and closed-orbit theory [6–9]. The signature of closed classical orbits has also been observed in sodium in an electric field [10], though this study was also limited to short-period orbits and was interpreted in terms of a semiclassical analysis of hydrogen.

We have found that lithium in an electric field provides an excellent system for studying how classical and quantum mechanics are related in a regime of chaos. Theoretically, the system is attractive because it is closely related to the hydrogen problem. Consequently, the effects of the difference with hydrogen—which leads to disorderly motion—can be observed in great detail. Experimentally, the system permits the high accuracy needed to generate detailed recurrence spectra for studying such phenomena as bifurcations, core scattering, and long-period orbits.

In Section II, we demonstrate that the classical motion undergoes a transition to chaos and that the energy-level fluctuations agree with the predictions of random matrix theory. In Section III, we review closed-orbit theory and discuss its applications to a one-electron atom in an electric field. Experimental methods are described in Sec. IV. In Secs. V and VI, we lay the foundation for interpreting the spectra in terms of the system's closed orbits. In Sec. VII, these results are applied to interpret behavior in the continuum, and in Sec. VIII they are applied to discrete spectra.

<u>51</u>   3604

Some results related to these studies have been reported previously. These are a study of the signature of very long-period orbits in the lithium Stark spectrum [11], and a detailed study of behavior in the vicinity of a bifurcation [12]. This paper includes details of those experiments and builds upon their results to more fully elucidate the connections between quantum and classical descriptions of lithium in an electric field.

II. CLASSICAL BEHAVIOR AND ENERGY-LEVEL STATISTICS

To introduce the lithium Stark problem, we present a classical description based on examination of the surfaces of section and a quantum description based on energy-level statistics. Both descriptions reveal disorderly behavior, but neither bridges the semiclassical regime that connects quantum and classical behavior. We will turn to that problem in Sec. III.

A. Classical motion

Hydrogen provides a natural starting point for understanding lithium Stark behavior. The Hamiltonian of hydrogen in an electric field is separable in parabolic (or semiparabolic) coordinates, and the classical motion is orderly. In alkali-metal atoms, however, the valence electron experiences a potential that deviates from $1/r$ near the origin due to the charge distribution of the inner electrons. Although this core potential is spherically symmetric, in an applied electric field it prevents the separation of variables. As a result, the motion is chaotic in certain regimes of energy and field.

The Hamiltonian of hydrogen in an electric field F in the z direction is taken to be (atomic units)

$$H = \frac{p^2}{2} - \frac{1}{r} + Fz. \tag{1}$$

The Hamiltonian is cylindrically symmetric, so L_z is conserved. The classical analysis is greatly simplified by scaling the Hamiltonian using the substitutions $r = F^{-1/2}\tilde{r}$ and $p = F^{1/4}\tilde{p}$. The scaled Hamiltonian $\tilde{H} = F^{-1/2}H$ does not explicitly depend on the field. Consequently, the classical dynamics depends only on the scaled energy $\epsilon = EF^{-1/2}$, not on E and F separately. This scaling rule can be employed to characterize the motion at all fields from consideration of the motion at a particular field.

Separation of variables can be accomplished using semiparabolic coordinates: $u = (r+z)^{1/2}$, $v = (r-z)^{1/2}$ [13]. The Hamiltonian (for $L_z = 0$) is

$$H = \frac{1}{2(u^2+v^2)}(p_u^2 + p_v^2 - 4) + \frac{1}{2}F(u^2 - v^2). \tag{2}$$

For numerical computations, a "regularized" Hamiltonian, $h = (u^2 + v^2)(H - E) + 2$, is introduced to remove the singularity:

$$h = \frac{p_u^2}{2} + \frac{p_v^2}{2} + \frac{1}{2}F(u^4 - v^4) - E(u^2 + v^2) = 2. \tag{3}$$

The regularized "energy" is always equal to two; the real energy, E, enters h as a parameter. For $F = 0$ and $E < 0$, the regularized Hamiltonian describes two uncoupled oscillators, both having frequency $\omega = (-2E)^{1/2}$. The electric field introduces anharmonic terms but does not couple the oscillators. Consequently, the motion remains separable in an electric field and is quasiperiodic. This reflects the existence of a third constant of motion [14] related to the Runge-Lenz vector $\mathbf{A} = (\mathbf{p} \times \mathbf{L}) - \mathbf{r}/r$. This constant of motion is $\mathbf{F} \cdot \mathbf{C}$, where $\mathbf{C} = \mathbf{A} - (\mathbf{r} \times \mathbf{F}) \times \mathbf{r}/2$.

Turning now to lithium, the Hamiltonian is

$$H = \frac{p^2}{2} - \frac{1}{r} + Fz + V_c(r), \tag{4}$$

where $V_c(r)$ describes the deviation from the $1/r$ potential at short distances where the two $1S$ electrons of the ionic core fail to completely screen the nucleus. Both the classical and quantum properties of the system are sensitive only to the coarse properties of the core potential, not to its detail. In the quantum solution, the core potential introduces a phase shift in the radial wave function that expresses itself as a quantum defect. The principal quantum number becomes $n^* = n - \delta_l$, where the quantum defect δ_l depends on the angular momentum but varies only slowly with energy.

The quantum defect has no strict classical counterpart because classical angular momentum is not quantized. However, if $\delta_l \gg \delta_{l+1}$, as in the case of lithium, a Kepler orbit with angular momentum $L = l + 1/2$ precesses through an angle of approximately $2\pi\delta_l$ every time it passes near the nucleus. We have found that the generic classical behavior does not depend strongly on details of the core but only on the size of the quantum defects. We employ a core potential of the form

$$V_c(r) = -\frac{(Z-1)e^{-ar}}{r}, \tag{5}$$

where $Z = 3$ is the nuclear charge and a is chosen to give the best agreement with measured quantum defects. $a = 2.13$ yields $\delta_s = 0.4$ and $\delta_p = 0.06$. The actual values are $\delta_s = 0.4$ and $\delta_p = 0.05$. (A two-parameter potential would exactly produce both quantum defects, but such exact agreement is unimportant when considering the amount of chaos in the system.)

Because of the core potential, the Runge-Lenz vector $\mathbf{A}$ is no longer an exact constant of motion for zero field, and $\mathbf{C} \cdot \mathbf{F}$ is not conserved once the field is applied. Regular motion requires at least as many constants of motion as degrees of freedom. In zero field, the energy and all three components of the angular momentum are conserved, and the motion is regular. In an electric field, only E and L_z are conserved. At low fields, the motion can be quasiperiodic, but it becomes chaotic as the field is increased.

The quasiperiodic trajectories of hydrogen form regular patterns in phase space. The trajectories of lithium follow the hydrogenic trajectories in the region outside the core. However, nearly every trajectory eventually passes through the core, at which point it is abruptly scattered into some other hydrogenic trajectory. Succes-

sive scattering from one hydrogenic trajectory to another can allow a trajectory to explore all of the phase space that is energetically available to it. Consequently, the core can induce ergodic or nearly ergodic behavior.

The development of chaos in lithium with increasing scaled energy is illustrated in the Poincaré surfaces of section in Fig. 1. These display $L_z = 0$ trajectories for lithium in semiparabolic coordinates. The curves are the loci of orbits in the (v, p_v) plane as they pass through the $u = 0$ plane. (Although the classical scaling rule, which is exact for hydrogen, is not strictly valid for lithium, it remains a useful approximation for examining the de-
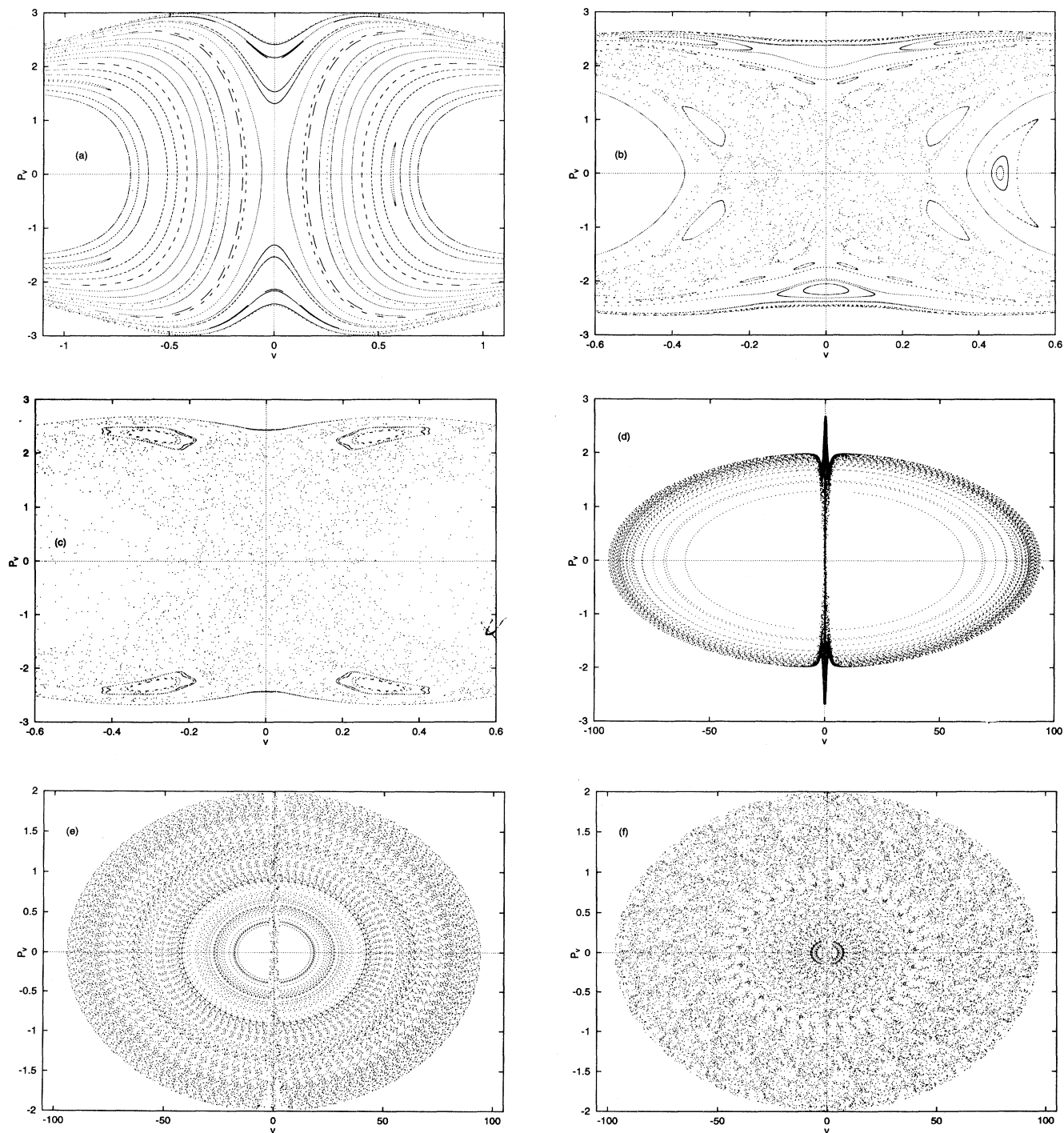

FIG. 1. Poincaré surfaces of section for lithium $E = -50\,\text{cm}^{-1}$, $L_z = 0$, and (a) $\epsilon = -32$; (b) $\epsilon = -16$; (c) $\epsilon = -12$; (d) $\epsilon = -12$; (e) $\epsilon = -8$; (f) $\epsilon = -4$; (g) $\epsilon = -3$; (h) $\epsilon = -2$.
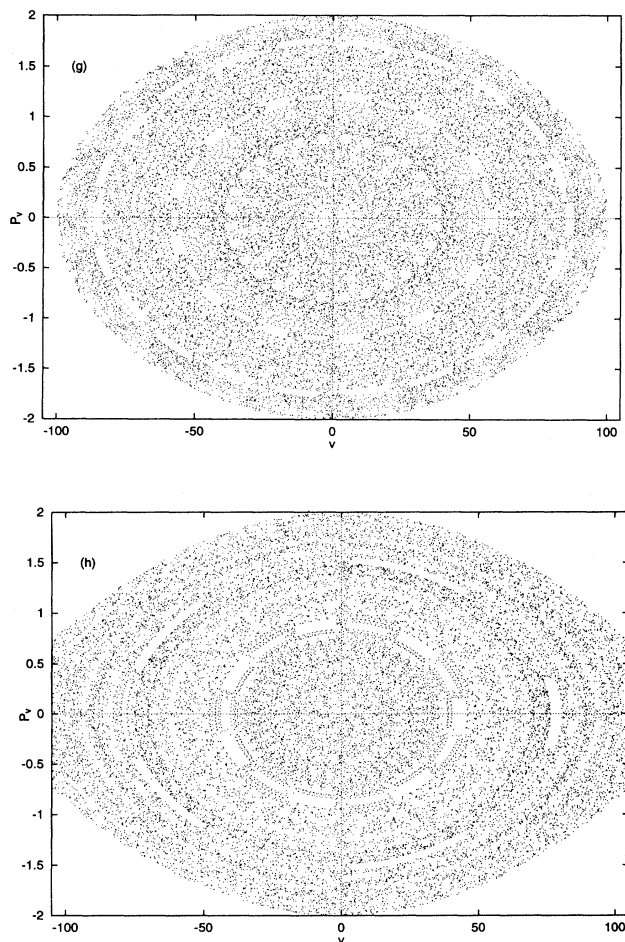
FIG. 1. (Continued).

B. Energy-level statistics

Energy-level statistics provide a characteristic signature of classical dynamics in quantum systems [15–17]. It is thought that regular classical dynamics is manifested by a Poisson distribution of energy levels, while for systems that display chaotic classical motion, the energy-level fluctuations are characterized by the statistics of random matrix eigenvalue ensembles.

For systems invariant under time reversal, the energy-level statistics of a number of chaotic systems have been shown to be in good agreement with the predictions of the Gaussian orthogonal ensemble of random matrices [7, 16]. It has been conjectured that this phenomenon is generic for all chaotic systems with this symmetry [18].

The nearest-neighbor distribution, $P(s)$, is a commonly used measure of the level repulsions which are associated with chaotic dynamics. If the normalized spacing between two energy levels is s, the normalized distribution of spacings for a chaotic system is well approximated by the Wigner distribution

$$P(s) = \frac{\pi}{2} s e^{-\frac{\pi}{4} s^2}. \tag{6}$$

In contrast, the normalized distribution of spacings for an orderly system is Poisson.

We have studied the nearest-neighbor distributions of hydrogen and lithium in an electric field by using spectra that were computed by standard methods [19, 20]. As expected, hydrogen displays nearly Poisson behavior in regions where levels from several n's (the principle quantum number at zero field) are mixed and below $\epsilon = -2$. Fig. 2(a) shows $P(s)$ for hydrogen at $\epsilon = -3$. In contrast, lithium exhibits nearly complete classical chaos for all scaled energies where several n's are mixed. We find that $P(s)$ is Wignerlike for $\epsilon = -3$, -2.5, and -2, as shown in Fig. 2(b)–2(d).

At $\epsilon = -3$ [Fig. 2(b)], $P(s)$ displays a slight enhancement compared with the Wigner distribution near $s = 0.8$, probably because three n's are barely mixed in

velopment of chaos.) Surfaces of section are computed for increasing values of F at $E = -50$ cm^{-1} with the value of scaled energy ranging from $\epsilon = -32$ to $\epsilon = -2$ (the classical ionization limit). At low scaled energy, the motion is regular and the orbits are quasiperiodic. The closed curves are cross sections of tori in phase space. The orbits wind around these tori, slowly covering them. For $\epsilon = -32$ [Fig. 1(a)], the motion is regular, and all tori are intact. At $\epsilon = -16$ [Fig. 1(b)] the tori have started to disintegrate and both disorderly and orderly regions are visible. At $\epsilon = -12$ [Fig. 1(c)], only a few tori are visible in the core region. The entire surface of section at that energy is shown in Fig. 1(d). The dotted curves look like tori, but they are not. As explained earlier, the electron is scattered from one hydrogenic torus to another whenever it passes through the core. (The lobes near $v = 0$ are caused by the attractive core expanding the volume of energetically available phase space. These lobes are present in all of the surfaces of section but are not shown at the higher scaled energies.) At $\epsilon = -8$ [Fig. 1(e)], island chains of tori are visible. At $\epsilon = -4$ [Fig. 1(f)], the regions supporting tori are very small. At $\epsilon = -3$ [Fig. 1(g)] and -2 [Fig. 1(h)], small regular regions remain, though most of the phase space is chaotic.
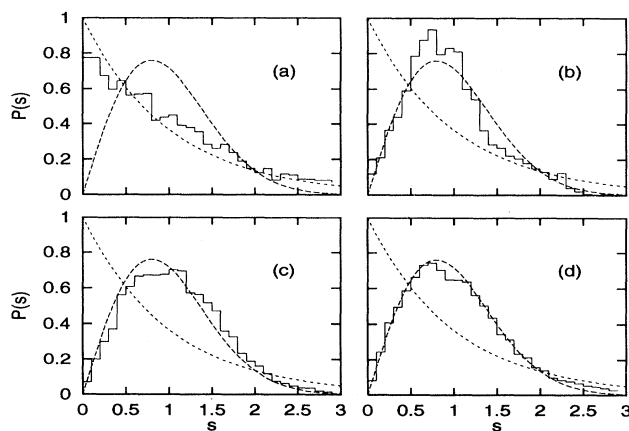

FIG. 2. Nearest-neighbor distributions of Stark energy levels for (a) hydrogen, $m = 0$, $\epsilon = -3$; (b) lithium, $m = 0$, $\epsilon = -3$; (c) lithium, $m = 0$, $\epsilon = -2.5$; (d) lithium, $m = 0$, $\epsilon = -2.0$. Short-dashed line is the Poisson distribution, and the long-dashed line is the Wigner distribution.

the region where the spectra were computed. By $\epsilon = -2$, approximately seven n's are mixed, and $P(s)$ shows much closer agreement with the Wigner distribution, as shown in Fig. 2(d).

These nearest-neighbor distributions display the familiar behavior and provide a convenient way to quantify spectral properties of many eigenvalues. However, they give little insight into either the underlying quantum structure or the classical dynamics. In contrast, closed-orbit theory provides a firm foundation for relating spectral correlations directly to classical trajectories.

III. CLOSED-ORBIT THEORY

A. The role of closed orbits

Spectral structures can display clear recurrences—periodicities associated with quantum wave packets that follow classical orbits. The periodic-orbit theory of Gutzwiller [4] and the closed-orbit theory developed by Delos and co-workers [5, 9, 13] provide the theoretical framework and the practical tools for relating spectral features to classical trajectories. At a deeper level, they provide a bridge between the quantum and classical worlds, even when the classical behavior is chaotic.

Periodic-orbit theory asserts that in a conservative system every periodic orbit produces a sinusoidal modulation in the density of states. Closed-orbit theory asserts that every orbit that is closed at the nucleus produces a sinusoidal modulation in the transition probability from a low-lying state to a high-lying state in the semiclassical regime, most generally a Rydberg state. Consequently, the Fourier transform of a quantum spectrum establishes a direct connection between quantum structure and classical dynamics.

According to closed-orbit theory [13], the photoabsorption cross section consists of a smooth background plus an oscillatory sum,

$$Df' = \sum_k \sum_{n=1}^{\infty} D_{nk} \sin(2\pi n w \tilde{S}_k - \Phi_{nk}), \qquad (7)$$

where k runs over all of the primitive closed orbits and n runs over their repetitions. $\tilde{S}_k = S_k/(2\pi w)$ is the scaled action of the first repetition of a closed orbit, where $w = F^{-1/4}$ is the scaled field. D_{nk} is the recurrence amplitude of the closed orbit. It contains information about the stability of the orbit, its initial and final angles, and the matrix element of the dipole operator between the initial state and a zero-energy Coulomb wave. Φ_{nk} is an additional phase that is computed from the Maslov index and geometrical considerations. The square of the recurrence amplitude D_{nk} is the recurrence strength.

Using closed-orbit theory to compute a spectrum with resolution ΔE requires summing over all closed orbits with periods up to $2\pi\hbar/\Delta E$. The theory has been applied with considerable success to low-resolution spectra where only short-period orbits need to be considered [9, 21]. However, extending the theory to high resolution presents a formidable challenge. The number of orbits grows rapidly with period or action. Furthermore,

for chaotic systems, long-period orbits are difficult to compute because they become increasingly unstable [4]. However, we will see that closed-orbit theory avoids this difficulty for the lithium Stark system by using the classical trajectories of hydrogen and a quantum model of core scattering.

B. Behavior at bifurcations

For $\epsilon > 0$, the lithium Stark system has only a single primitive closed orbit. This is the "uphill" orbit along the z axis. As the energy is decreased, new orbits spring into existence by an orderly sequence of bifurcations. In many systems, bifurcations give rise to the proliferation of periodic orbits that characterizes chaotic systems. The original formulation of closed-orbit theory predicts that the recurrence strength is proportional to the density of neighboring orbits when a closed orbit returns to the nucleus. This prediction is valid far from a bifurcation, but the density of returning neighbors becomes infinite at a bifurcation, and the predicted recurrence strength diverges [13]. Such divergences are familiar in geometrical optics, which predicts infinite intensity if a plane wave is focused to a point. These theories are corrected by accounting for diffraction. Gao and Delos have modified closed-orbit theory to include such diffraction effects. Data taken as part of these studies has confirmed their description [12].

C. Core scattering

Chaos that results from core scattering in lithium is qualitatively different from chaos in diamagnetic hydrogen. In the case of the diamagnetic hydrogen atom [6], the irregular motion arises from the interplay of fields with different symmetries: motion is dominated at short distances by the spherical Coulomb interaction and at large distances by the cylindrical diamagnetic interaction. In lithium in an electric field, chaos arises from the alkali-metal core, which is a small structure compared with the size of Rydberg atoms.

Classically, the effect of the lithium core is dramatic because trajectories can explore arbitrarily small regions of phase space. In contrast, quantum mechanics tends to smooth over such regions. The generation of recurrences by scattering of waves by the ionic core in alkali metals provides a quantum mechanical analog to the scattering of trajectories discussed in Sec. II. In the classical system, the core causes chaos by scattering an orbit from one hydrogenic trajectory into another each time it passes near the nucleus. Closed-orbit theory treats core scattering quantum mechanically [21]. For a pure $1/r$ potential, an incoming wave following a closed orbit is backscattered and propagates from the nucleus in the same direction from which it came. For potentials that deviate from $1/r$, the scattering process is described using a partial wave expansion of the incoming recurrence. The incoming wave is not only backscattered, but a component of the wave is also scattered outward in all directions. Upon reaching distances where the semiclassical approximations are valid, this wave then propagates

along all of the closed orbits of the system. Consequently, recurrences occur not only at the scaled actions of hydrogenic closed orbits, but also at the sum of actions of any combination of closed orbits. Such core-scattered recurrences have been identified in the odd-parity spectrum of diamagnetic helium [22]. The role of core scattering in diamagnetic recurrence spectra has been studied by Dando et al. [23]. As will be shown, the lithium system allows core-scattered recurrences to be precisely identified.

D. Scaled-energy spectroscopy of lithium in an electric field

Every closed orbit contributes an oscillatory component to the absorption spectrum. The signature of each closed orbit is a peak in the Fourier transform of a spectrum taken at constant scaled energy as a function of $F^{-1/4}$. Such a transformed spectrum is called a recurrence spectrum.

In principle, each peak in a recurrence spectrum lies at the scaled action of a closed orbit, and its height is proportional to that orbit's recurrence strength. (In practice, overlapping peaks can interfere with each other.) This method, called scaled-energy spectroscopy, was used by Holle et al. to interpret the spectrum of diamagnetic hydrogen [8]. It has since been applied to the spectra of sodium in an electric field [10], and in diamagnetic helium [24].

We have studied the recurrence spectra of lithium in an electric field experimentally and computationally in order to study the role of core scattering in inducing quantum chaos and the role of bifurcations in governing spectral evolution, and also to investigate recurrences corresponding to long-period orbits. Before discussing these spectra, we briefly describe the techniques by which they were obtained.

IV. EXPERIMENTAL METHOD

The experimental goal is to acquire high-resolution and high-accuracy photoabsorption spectra at constant scaled energy. The lasers and field are varied simultaneously so as to keep the scaled energy—and hence the classical dynamics—constant [8, 10]. High resolution is needed to observe long-period orbits; high accuracy is needed for detailed comparison with quantum and semiclassical predictions.

Our experiment employs a lithium atomic beam that passes through apertures in the centers of a pair of electric field plates, as shown in Fig. 3. Between the field plates, the atoms are excited to Rydberg states by laser light and are then detected by electric field ionization. One laser excites the $2S \rightarrow 3S$ two-photon transition and a second laser excites Rydberg states.

A lithium atomic beam emerges from a conventional oven and passes through apertures on the axis of two disk-shaped field plates. This geometry permits measurement of photoabsorption spectra for both bound and unbound states. The plate voltages are arranged so that if ionization occurs in the interaction region, the ions are
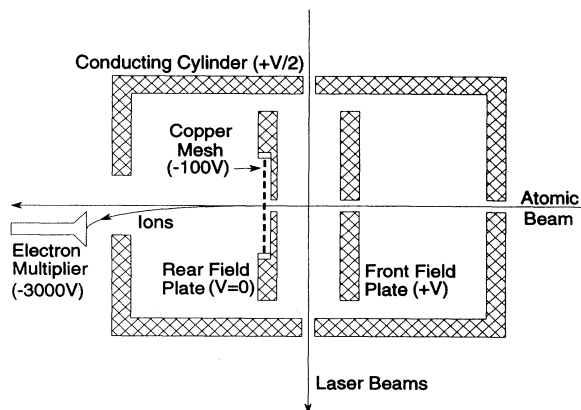

FIG. 3.   Experimental interaction region.

accelerated toward the detector. If bound Rydberg states are excited, the atoms drift into a region where a copper mesh at -100 V placed 3 mm behind the grounded rear field plate generates a field sufficient for ionization.

The lithium is excited by a stepwise process. Atoms are excited from the $2S$ to the $3S$ state by a two-photon transition at 735.130 nm. The laser power is typically 1 W. The population of $3S$ atoms is monitored by cascade fluorescence from the $2P \rightarrow 2S$ transition at 671 nm collected in a plexiglass light pipe and measured with a photomultiplier. A second dye laser provides light near 620 nm for exciting Rydberg states. The power of this laser is typically 200 mW. Lithium ions are detected with a channel electron multiplier. The ion signal is corrected for variations in the laser power and the fluorescence signal which indicates the number of $3S$ atoms.

Precision measurement of the 620 nm laser frequency is accomplished by recording an iodine absorption spectrum and the transmission of a calibrated etalon as the laser is scanned. The frequencies of all the iodine absorption lines in the regions studied are known to an accuracy of $5 \times 10^{-4}\,\mathrm{cm}^{-1}$ [25, 26]. The frequencies of the iodine spectra have been checked by comparison with zero-field Rydberg spectra and some slight adjustments have been made. The etalon transmission peaks are used to extrapolate the frequency of each point in a scan from a given iodine line. The accuracy of this assignment is limited primarily by the uncertainty in tabulated frequencies of the iodine absorption lines and the uncertainty in the measured position of the minimum of the absorption line. Energies are typically determined to better than $1 \times 10^{-3}\,\mathrm{cm}^{-1}$, which is close to the spectral resolution of the experiment.

The experimental resolution of 30 MHz is limited by several effects of comparable magnitude. Doppler broadening contributes roughly 12 MHz. The finite time the atom spends in the laser path contributes about 10 MHz. The natural linewidth of the $3S$ level contributes 8 MHz. The laser linewidth is about 1 MHz.

The largest sources of error in the scaled-energy spectra arise from the uncertainty in the electric field calibration and the inhomogeneity of the field over the in-

teraction volume. The electric field was calibrated in terms of the voltage across the field plates by comparing Stark splittings of the $n = 31$ manifold with computed energy level separations using fields near 50 V/cm. The fractional error in the field-to-voltage ratio obtained in this way was typically less than 0.1%. We studied the inhomogeneity of the electric field over the interaction volume by observing the broadening of highly sloped levels in the $n = 31$ manifold. The interaction volume is the intersection of the laser and atomic beams. It is typically 3 mm long and 50 μ in diameter. The observed field inhomogeneity was consistent with numerical models of the interaction region. For 64 mm diameter plates with 3 mm apertures separated by 19 mm, the contribution to the width of a spectral line due to the field inhomogeneity was 0.1% of the Stark shift. This separation was used for experiments with $\epsilon < -2$. Experiments with $\epsilon > -2$ were performed with a separation of 13 mm, which yields a broadening of about 0.3% of the Stark shift.

Measuring a constant scaled energy spectrum is accomplished by first scanning the laser at 620 nm over the desired interval while recording the iodine absorption and etalon transmission. This information is used to compute the energy of every point in the scan. The laser is scanned a second time while the proper voltage is applied to the field plates so that the desired scaled energy is maintained. Each scan covers 0.7 cm^{-1}. A constant scaled energy spectrum typically covering 15 cm^{-1} is obtained by concatenating scans from adjacent energy ranges. The error in setting the energy to maintain constant scaled energy is 0.002 cm^{-1}. For spectra with $\epsilon \geq -2$, the fractional error in the electric field is 0.3% which gives a fractional error in the scaled energy of 0.15%. For spectra with $\epsilon < -2$, the fractional error in the electric field is 0.1% which results in a fractional error in the scaled energy of 0.05%.

V. THE CLOSED ORBITS OF HYDROGEN

To provide a framework for understanding the recurrence spectra of the lithium Stark system, we describe the closed orbits of the hydrogen Stark problem. As explained by Gao and Delos [13], the quasiperiodic motion of a given trajectory can be analyzed in terms of the motion along the u and v axes. The regularized Hamiltonian of hydrogen in an electric field (Eq. 3) can be separated by inspection yielding

$$h_u = \frac{p_u^2}{2} + \frac{1}{2}Fu^4 - Eu^2 = e_u \qquad (8)$$

and

$$h_v = \frac{p_v^2}{2} - \frac{1}{2}Fv^4 - Ev^2 = e_v, \qquad (9)$$

where e_u and e_v are separation constants subject to the constraint $e_u + e_v = 2$.

By definition, closed orbits begin at the origin. If θ_0 is the initial angle of the orbit with respect to the u axis, the periods of u and v motion are

$$T_u = 2 \int_0^{u_{max}} \frac{du}{\sqrt{4\cos^2\theta_0 - Fu^4 + 2Eu^2}} \qquad (10)$$

and

$$T_v = 2 \int_0^{v_{max}} \frac{dv}{\sqrt{4\sin^2\theta_0 + Fv^4 + 2Ev^2}}, \qquad (11)$$

where u_{max} and v_{max} are the classical turning points of the u and v motion. The scaled periods are obtained by making the substitutions $F = 1$ and $E = \epsilon$.

For $\epsilon > 0$ the motion is unbounded. The only closed orbit, the uphill orbit, lies on the u axis (positive z axis), with $\theta_0 = 0$. This orbit, which is unstable for $\epsilon > 0$, is confined between the origin and the classical turning point in the barrier of the applied field. The shortest uphill orbit is denoted by U_1 and its repetitions by U_n, where n is the repetition number.

For $\epsilon < 0$, bound orbits are possible for $\theta_0 > 0$. As the scaled energy is lowered from $\epsilon = 0$ to $\epsilon = -2$, the largest initial angle for which the motion is bounded grows from $\theta_0 = 0$ to $\theta_0 = \pi/2$ in semiparabolic coordinates. For $\epsilon \leq -2$, the orbit on the v axis (negative z axis), the "downhill" orbit, is closed. The shortest downhill orbit is denoted by D_1 and its repetitions by D_n.

Among all the possible trajectories which begin at the origin, those for which the ratio of T_u to T_v is rational constitute closed orbits. Since $T_u \leq T_v$, the maximum ratio is 1. The locus of allowed trajectories is indicated by the shaded region in Fig. 4.

As ϵ is lowered below 0, the uphill orbit becomes stable and other closed orbits begin to be born by bifurcations of repetitions of the uphill orbit. Consider, for instance, the closed orbit with period ratio $T_u/T_v = 1/2$, which bifurcates from U_2 at $\epsilon \approx -0.4$. At the bifurcation energy, the 1/2 orbit is tangential to the u axis ($\theta_0 = 0$), and has the same period as U_2. As the energy decreases below the bifurcation energy, the initial angle of the 1/2 orbit increases until it reaches $\theta_0 = \pi/2$ at an energy just below $\epsilon = -2$, where the orbit abruptly disappears. With the exception of the uphill and downhill orbits, all closed orbits are created and destroyed on the boundaries of the allowed region in Fig. 4. As ϵ is lowered, closed orbits are created at the upper boundary and destroyed at the lower boundary. Conversely, as ϵ is raised, closed orbits are created at the lower boundary and destroyed at the upper boundary.

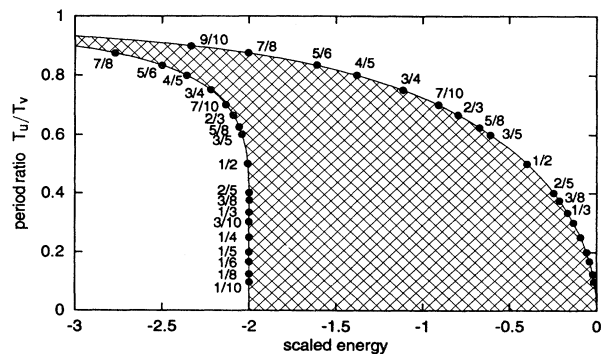An example of this process is shown in Fig. 5, which il-

FIG. 4. Ratio of periods T_u/T_v as a function of scaled energy. The region of allowed period ratios is shaded. Bifurcations occur at the edges of this region.
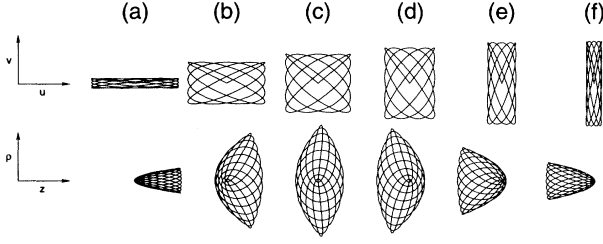
FIG. 5. Pictures of the 9/10 orbit as the scaled energy changes. Top row: semiparabolic coordinates. Bottom row: cylindrical coordinates. (a) $\epsilon = -2.35$; (b) $\epsilon = -2.50$; (c) $\epsilon = -2.65$; (d) $\epsilon = -2.80$; (e) $\epsilon = -2.95$; (f) $\epsilon = -3.00$.

lustrates the behavior of the 9/10 orbit. It is displayed in the (u, v) semiparabolic coordinates and in the more familiar (ρ, z) cylindrical coordinates. As the scaled energy is lowered through $\epsilon = -2.342$, the maximum allowed period ratio goes through 9/10 and the orbit is born by bifurcation of U_{10}. As ϵ is lowered, the initial angle increases and the orbit progressively changes shape. This orbit exists until the minimum allowed period ratio goes through 9/10 and the orbit is destroyed by a collision with D_9 (on the $-z$ axis) at $\epsilon = -3.025$.

Finding closed orbits at a given scaled energy is a simple matter of computing the period ratio of orbits launched from the origin at various initial angles. Because the period ratio is a slowly varying function of θ_0, it is easy to converge upon any desired ratio by a simple iterative procedure.

VI. RECURRENCE SPECTRA

Relating closed orbits to recurrence spectra requires knowing their action. For a closed orbit of hydrogen, the action is $S_H = S_u + S_v$, where

$$S_u = 2 \int_0^{u_{max}} \sqrt{4 \cos^2 \theta_0 - Fu^4 + 2Eu^2} \, du \qquad (12)$$

and

$$S_v = 2 \int_0^{v_{max}} \sqrt{4 \sin^2 \theta_0 + Fv^4 + 2Ev^2} \, dv. \qquad (13)$$

The scaled actions are obtained by the substitutions $F = 1$ and $E = \epsilon$, except that by convention the scaled action $\tilde{S}$ is divided by 2π.

The scaled action of the uphill parallel orbit is

$$\tilde{S}_H = \frac{1}{\pi} \int_0^{\tilde{z}_{max}} \left[2\left(\epsilon + \frac{1}{\tilde{z}} - \tilde{z}\right) \right]^{1/2} d\tilde{z}, \qquad (14)$$

where $\tilde{z}_{max}$ is the classical turning point. Similarly, the scaled action of the downhill parallel orbit is

$$\tilde{S}_H = \frac{1}{\pi} \int_0^{\tilde{z}_{min}} \left[2\left(\epsilon + \frac{1}{\tilde{z}} - \tilde{z}\right) \right]^{1/2} d\tilde{z}, \qquad (15)$$

where $\tilde{z}_{min}$ is the classical turning point.

To interpret the recurrence spectra of lithium in an

electric field, we need to take into account the failure of the classical scaling rule in the core region. As explained in the Appendix, the action can be written, $S = 2\pi(w\tilde{S}_H + \delta_s)$, where $\tilde{S}_H$ is the scaled action of the same closed orbit in hydrogen, and δ_s is the s-state quantum defect. Consequently, the frequency of the modulation a closed orbit adds to the spectrum is the hydrogenic scaled action, and the contribution of the core is a constant phase. We expect the position of peaks in the lithium recurrence spectrum to be given by the scaled actions for hydrogen.

In the next two sections, we use experimental and computed recurrence spectra to show that the spectral evolution has a natural and intuitive interpretation in terms of closed orbits. In the continuum regime ($\epsilon > -2$), the spectrum is dominated by the uphill orbits and their bifurcations. In the discrete regime ($\epsilon < -2$), several other effects are visible, including new recurrences due to core scattering and the downhill orbits and their bifurcations.

VII. RECURRENCE SPECTRA IN THE CONTINUUM REGION

At large positive energies, the photoabsorption spectrum of single-electron atoms in an electric field displays a single sinusoidal oscillation [27]. For $E > 0$, the only closed orbit is the uphill parallel orbit. The spectrum contains a fundamental Fourier component from this orbit (U_1) plus harmonics from its repetitions (U_n). U_1 is unstable for $\epsilon > 0$, and none of its neighbors returns to the nucleus. As a result, the amplitude of the harmonics decreases roughly exponentially [13]. Just above $E = 0$, many harmonics contribute, and the spectrum resembles a sawtooth. The exponential decay rate increases as ϵ is increased, resulting in a single sinusoid at large positive energy [27, 21].

A study of the low-action recurrences in continuum Stark spectra reveals recurrences corresponding to the uphill parallel orbits. Whenever a new orbit is created by a bifurcation, there is a large increase in recurrence strength. At scaled energy below the bifurcation energy, the newly created orbit has scaled action slightly lower than the parent uphill orbit, U_n, and the recurrence is shifted to lower action. This bifurcation shift becomes especially apparent in the high-action recurrence spectra.

A. Low-action recurrence spectra in the continuum region

Computed values of the scaled actions of U_1 and its repetitions are plotted as a function of ϵ in Fig. 6(a). The bifurcations (also shown in Fig. 4) are marked and labeled with the period ratio of the newly created orbit. Fig. 6(b) shows the experimental recurrence spectrum for $\epsilon = -1.6$. The recurrence strength is plotted on the scaled-energy axis in arbitrary units. As expected, the recurrence spectrum displays peaks at every repetition of the parallel orbit. The recurrence strength varies widely and is large for U_5, U_6, and U_{11}. This is because the 4/5, 5/6, and 9/11 bifurcations occur at scaled energies near
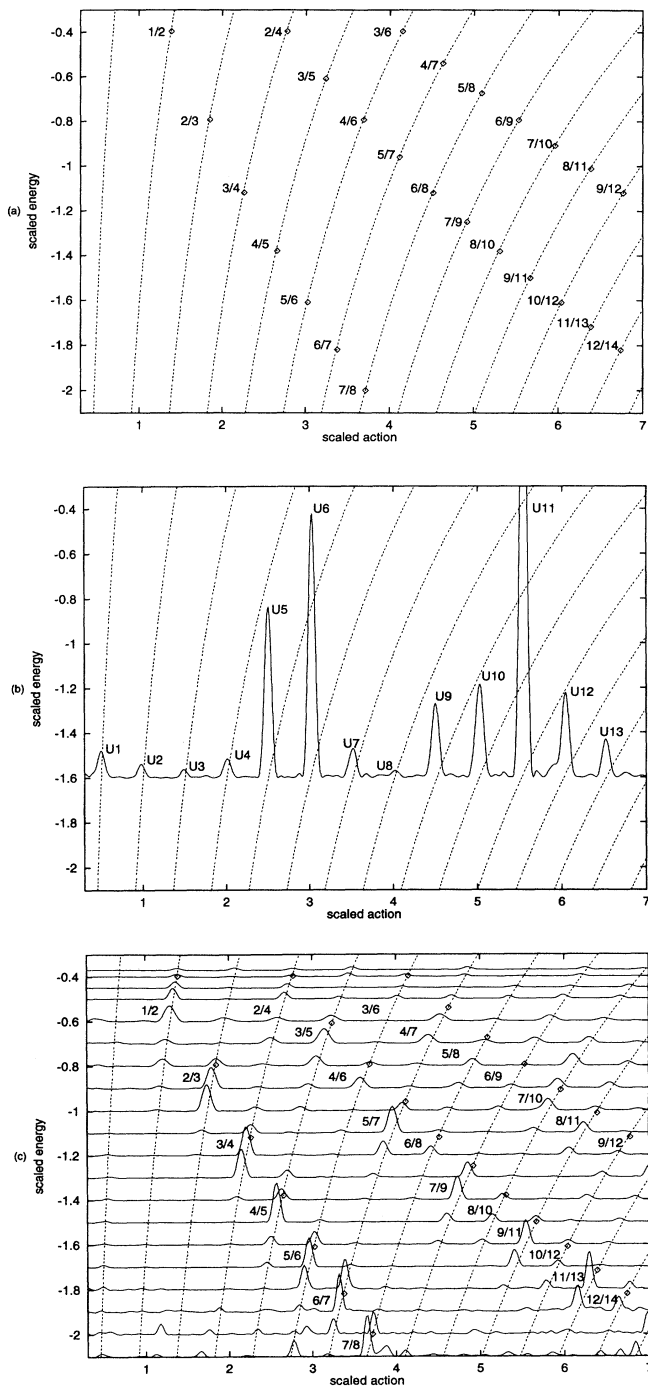
FIG. 6. (a) The scaled action of repetitions of the uphill parallel orbit U_n as a function of scaled energy. The primitive orbit is the lowest action curve, and the other curves are successive repetitions. Points where bifurcations occur are labeled with the period ratio of the newly created orbit. (b) Experimental recurrence spectrum for $\epsilon = -1.6$. The recurrence strength is plotted on the scaled-energy axis in arbitrary units. Each peak corresponds to a repetition of the parallel orbit. (c) Experimental recurrence spectra for $-2.1 \leq \epsilon \leq -0.37$. As the scaled energy decreases, the recurrence strength begins to increase just before a bifurcation and reaches a maximum slightly after a bifurcation.

$\epsilon = -1.6$.

To show how the recurrence spectrum evolves from $\epsilon = 0$ to the classical ionization threshold, we have reduced the recurrence spectrum at $\epsilon = -1.6$ by a factor of 20 and formed a map of experimental recurrence spectra for $-2.1 \leq \epsilon \leq -0.37$. Figure 6(c) displays the results. The scaled actions of most peaks correspond to repetitions of the uphill parallel orbit. However, they are only large enough to be seen in the plot in the vicinity of a bifurcation.

The evolution of these recurrence strengths follows a general pattern as ϵ is varied. As the scaled energy approaches the bifurcation from above, the recurrence strength increases significantly. The uncertainty principle allows the quantum system to "see" the bifurcation before it occurs classically [28]. As the scaled energy passes through the bifurcation the recurrence strength increases rapidly, achieving its maximum value slightly after the bifurcation. This large increase in recurrence strength is the result of the focusing of the incoming wave nearly to a point at the bifurcation.

At a bifurcation, the parent and the newly created orbit have identical actions. For scaled energies slightly below a bifurcation (where the recurrence is large), the newly created orbit carries most of the recurrence strength. Its action is slightly less than that of the repetition of the uphill orbit from which it bifurcated. These two actions are not far enough apart for distinct peaks to be resolved, but the dominance of the newly created orbit shifts the peak position slightly from the scaled action of the repetition.

To illustrate this bifurcation shift, we consider the recurrence spectrum at $\epsilon = -1.6$ which is shown in Fig. 6(b). Only the large peaks will be considered because experimental noise prevents accurate determination of the position of the smaller peaks. The scaled action of the 5th peak is $\tilde{S}_{exp}(U_5) = 2.506(3)$, where the number in parentheses indicates the experimental error in the last digit. The classical action of U_5 is $\tilde{S}_{cl}(U_5) = 2.520$, which is higher than the experimental value. However, the $4/5$ orbit carries most of the recurrence strength. This orbit was created at $\epsilon = -1.38$, and at $\epsilon = -1.6$, its action is $\tilde{S}_{cl}(4/5) = 2.511$, which is almost within the experimental error of the measured value. In contrast, U_6 is not shifted by a newly created orbit, because the $5/6$ bifurcation does not occur until $\epsilon = -1.61$. $\tilde{S}_{exp}(U_6) = 3.027(3)$, and $\tilde{S}_{cl}(U_6) = 3.024$, as expected.

The U_9, U_{10} and U_{11} peaks at $\epsilon = -1.6$ are other examples of bifurcation shifted recurrences. U_9 is shifted the most because it is far from the $7/9$ bifurcation which occurs at $\epsilon = -1.25$. $\tilde{S}_{exp}(U_9) = 4.501(5)$. This agrees with $\tilde{S}_{cl}(7/9) = 4.493$, though not with $\tilde{S}_{cl}(U_9) = 4.536$. Similarly, $\tilde{S}_{exp}(U_{10}) = 5.024(5)$, agrees with $\tilde{S}_{cl}(8/10) = 5.022$, though not with $\tilde{S}_{cl}(U_{10}) = 5.040$. (The $8/10$ bifurcation occurs at $\epsilon = -1.38$.) In contrast, U_{11} at $\tilde{S}_{exp}(U_{11}) = 5.543(6)$ is not significantly shifted from $\tilde{S}_{cl}(U_{11}) = 5.544$ because the $9/11$ bifurcation is close ($\epsilon = -1.50$) and $\tilde{S}_{cl}(9/11) = 5.540$.

The bifurcations shown in Fig. 6 fall naturally into

three sequences. The first sequence has period ratios of
the form $n/(n+1)$. Such bifurcations include 1/2, 2/3,
3/4, etc. All of these bifurcations result in large recur-
rence strengths. The second sequence has period ratios of
the form $n/(n+2)$. Bifurcations that produce closed or-
bits whose periods are irreducible fractions are observed
to give stronger recurrence strengths than those asso-
ciated with reducible fractions. For example, the 3/5,
5/7, 7/9, 9/11, and 11/13 bifurcations produce larger
recurrences than the 2/4, 4/6, 6/8, 8/10, 10/12, and
12/14 bifurcations. (Orbits with reducible period ratios
are repetitions of the corresponding reduced fraction.)
The third sequence of bifurcations has period ratios of
the form $n/(n+3)$. This pattern of irreducible fractions
giving larger recurrences is also apparent in this sequence
of bifurcations.

Fig. 6(c) reveals an overall loss of recurrence strength
as ϵ is increased. This has a straightforward explana-
tion. For $\epsilon = -2.1$ the spectrum is discrete, and all
of the photoabsorption signal appears as peaks in the
Fourier transform. As the scaled energy is raised, the
continuum background grows and the photoabsorption
resonances become small peaks on a large background.
Consequently, most of the signal is piled up at zero fre-
quency in the Fourier transform.

B. High-action recurrence spectra in the continuum region

The pattern of peaks in the recurrence spectrum near
repetitions of the parallel orbit continues to high action
and provides the spectral signature of long period orbits.
Figure 7 shows a blowup [recurrence strengths multiplied
by a factor of 25 compared with Fig. 6(c)] of recurrence
spectra in the range $20 < \tilde{S} < 40$ and $-0.5 \leq \epsilon \leq -0.37$.
The dashed lines represent the actions of repetitions of
U_1. Most of the prominent peaks are at actions approx-
imately 4% below repetitions of the parallel orbit. We
attribute this to a bifurcation shift that pulls the scaled
action of recurrences to slightly lower action than the
parents from which they bifurcate.

For $\tilde{S} < 7$, the large increases in recurrence strength
could be associated with bifurcations. These matters are
more complicated at higher action. Because of the large
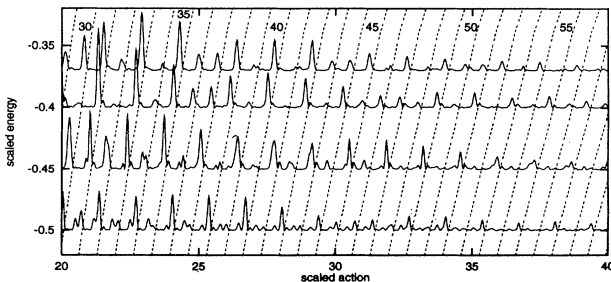denominators in the relevant period ratios, the density of

FIG. 7. Experimental recurrence spectra at large action
for $-0.5 \leq \epsilon \leq -0.37$. The dashed lines are the action of
repetitions of the parallel orbit. The numbers to the left of
the dashed line are the number of repetitions.

TABLE I. Scaled actions and bifurcation energies of orbits
contributing to the U_{45} recurrence at $\epsilon = -0.45$.

Orbit	$\tilde{S}$	ϵ_{bif}
U_{45}	30.58	
23/45	30.56	-0.42
22/45	30.56	-0.38
21/45	30.53	-0.34
20/45	30.52	-0.30
19/45	30.47	-0.28

bifurcations is much higher than at low action. For exam-
ple, in Fig. 7, the U_{45} recurrence is large for $\epsilon = -0.45$.
The newly created orbits that could contribute to it and
their actions are shown in Table I. The 23/45, 22/45,
21/45, 20/45, and 19/45 bifurcations have all just oc-
curred. The recurrence amplitudes of these new orbits
add coherently. The scaled action of U_{45} at $\epsilon = -0.45$
is $\tilde{S}_{cl}(U_{45}) = 30.58$ whereas the experimental position is
$\tilde{S}_{exp}(U_{45}) = 30.50(3)$. It appears that these recurrences
combine largely in phase. This would produce an ex-
perimental peak at an action slightly lower than that of
U_{45}. For the small recurrences in Fig. 7, a number of bi-
furcations also contribute large recurrence strengths, but
presumably these interfere destructively. We note that
the largest recurrences of the parallel orbit are odd for
$\epsilon = -0.45$ and even for $\epsilon = -0.5$, though we have no
simple explanation.

In addition to the recurrences corresponding to repe-
titions of the parallel orbit, a few extra peaks are visible
in the recurrence spectrum for $\epsilon = -0.37$. The number
of these additional peaks increases as the scaled energy
is decreased. These peaks arise from orbits that bifur-
cated from the parallel orbit and its repetitions. Such
newly created orbits are not visible as distinct peaks in
the low-action spectra shown in Fig. 6(c) because the ac-
tion of a newly created orbit is close to the action of its
parent. However, repetitions of many of these orbits are
resolved at the higher actions shown here.

We mention two other possibilities to explain why the
recurrences in Fig. 7 have scaled action approximately
0.4% less than the action of simple repetitions of the up-
hill parallel orbit. Such a regular displacement suggests
the possibility of a systematic error in the electric field
calibration. However, the discrepancy would require our
field calibration to be in error by 16 times our estimated
uncertainty. Furthermore, the bifurcation shift in Fig. 7
has been reproduced in separate measurements using sep-
arate field calibrations.

Another way to account for the displaced positions of
long-action recurrences is to compute the scaled action
for the parallel orbit by beginning and ending the orbit
at the core radius. This approach gives agreement with
the data, but does not seem rigorous. Procedures for
calculating the action are discussed in the Appendix.

VIII. RECURRENCE SPECTRA IN THE DISCRETE REGION

In the discrete region (below the classical ionization
threshold, $\epsilon = -2$), most peaks in the low-action recur-

rence spectrum of lithium lie at the classical actions of hydrogenic closed orbits. These peaks correspond to U_n, D_n, and orbits which bifurcate from them. However, there are additional peaks in the low-action recurrence spectra. These can be attributed to scattering from one hydrogenic orbit into another by the alkali-metal core. The spectral evolution can be interpreted in terms of bifurcations and core scattering. High-action recurrence spectra in the discrete region display peaks corresponding to many repetitions of the uphill parallel orbit, but their scaled action cannot be accounted for by a bifurcation shift, as in the continuum region.

A. Low-action recurrence spectra

1. Bifurcations

At low action, the bifurcations of repetitions of the uphill parallel orbit (U_n) continue to follow the same pattern as in the continuum regime. In addition, recurrences associated with the downhill parallel orbit and its repetitions (D_n) appear in the spectrum. (These orbits immediately ionize for $\epsilon > -2$.) The recurrence strength of these orbits follows the same pattern as the uphill recurrences near a bifurcation, except that the D_n bifurcate as the scaled energy is increased. The recurrence strength begins to increase just before the bifurcation and reaches its maximum slightly after the bifurcation. This behavior is shown in Fig. 8.

In the discrete region, spectra can be computed accurately using standard techniques [19]. Figure 9 compares the experimental recurrence spectrum at $\epsilon = -3$ with a recurrence spectrum obtained from quantum computations [29]. Agreement is generally good. Computing recurrence spectra makes investigation possible at scaled energies where experimental data is unavailable and makes it possible to compare with hydrogen. Fur-
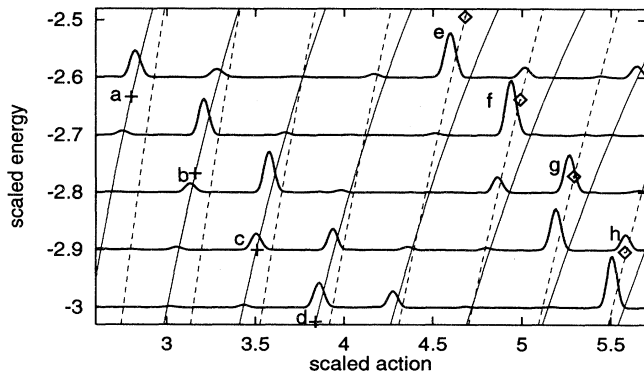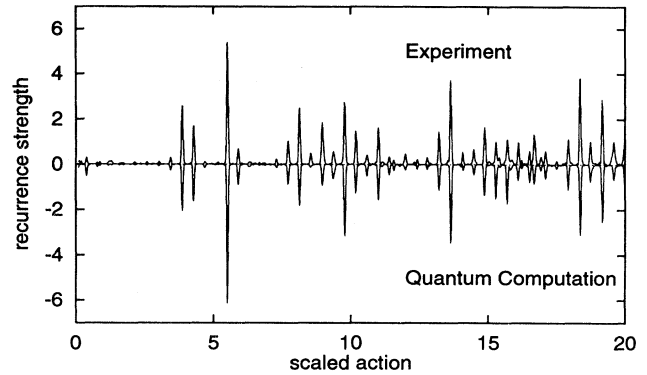

FIG. 9. Lithium recurrence spectrum for $\epsilon = -3$. A mirror plot is used for comparison of the experimental spectrum (top) with the results of a quantum computation (bottom). The normalization is arbitrary.

thermore, it permits studying the onset of chaos in the recurrence spectrum as the quantum defect is varied from $\delta_s = 0$ (hydrogen) to $\delta_s = 0.4$ (lithium).

2. Core-scattered recurrences

Figure 10 displays the experimental recurrence spectrum of lithium and the computed recurrence spectrum of hydrogen for $\epsilon = -3$. The lithium recurrence spectrum begins to show large differences from hydrogen for $\tilde{S} > 8$. In hydrogen, every peak in the recurrence spectrum corresponds to either repetitions of the parallel orbits or orbits that bifurcated from them. The prominent peaks in the hydrogenic spectrum are large because of a nearby bifurcation. (D_9 and D_{10} are large because of the nearby 9/10 and 10/11 bifurcations that occur at $\epsilon = -3.02$ and $\epsilon = -3.14$, respectively. U_{14} and U_{15} are large because they are close to the 13/14 and 14/15 bifurcations that occur at $\epsilon = -2.90$ and $\epsilon = -3.03$, respectively. D_{18} and D_{19} are close to the 18/20 and 19/21 bifurcations.)

In addition, several strong recurrences are evident in

FIG. 8. Bifurcations of D_n and U_n are visible in the experimental recurrence spectra for $-3 \leq \epsilon \leq -2.6$. The thin solid lines are the scaled actions of the D_n. The dashed lines are the scaled actions of the U_n. The two series of prominent peaks at low action correspond to the $n/(n+1)$ sequences of D_n and U_n bifurcations. Bifurcations of the downhill orbit are marked with crosses: (a) 6/7; (b) 7/8; (c) 8/9; (d) 9/10. Bifurcations of the uphill orbit are marked with diamonds: (e) 11/12; (f) 12/13; (g) 13/14; (h) 14/15.
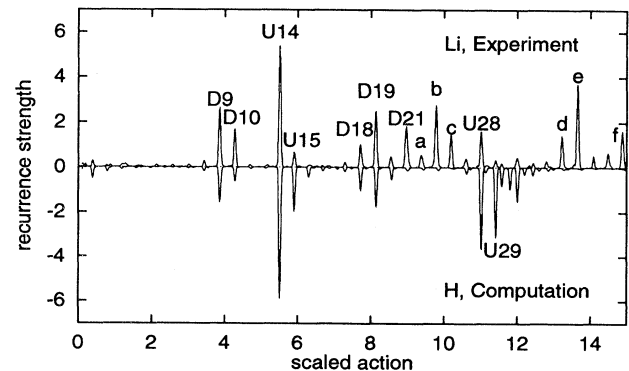

FIG. 10. Comparison of the recurrence spectra of lithium and hydrogen, $\epsilon = -3$. Top: experimental recurrence spectrum of lithium. Bottom: computed recurrence spectrum of hydrogen. The labels a through f denote core-scattered recurrences, as explained in the text and Table II.

TABLE II. Scaled actions $\tilde{S}$ of selected core-scattered recurrences in the experimental spectrum at $\epsilon = -3$ compared with the sum of the observed actions of their components, $\tilde{S}_{sum}$.

Label	Components	$\tilde{S}_{sum}$	$\tilde{S}$
a	$U_{14} + D_9$	9.364	9.357
b	$U_{14} + D_{10}$	9.782	9.784
c	$U_{15} + D_{10}$	10.177	10.193
d	$U_{14} + D_{18}$	13.222	13.224
e	$U_{14} + D_{19}$	13.641	13.641
f	$U_{15} + D_{21}$	14.872	14.882

the lithium spectrum that are not at the scaled action of a closed orbit. However, these can be identified as core-scattered recurrences because they occur at scaled actions that are the sum of the action of hydrogenic closed orbits. The largest core-scattered recurrences occur at actions that are the sum of large recurrences because the amplitude of a core-scattered recurrence is proportional to the amplitude of each of its components. Table II shows that the recurrences labeled a through f in Fig. 10 may be interpreted as effects of core scattering.

By computing recurrence spectra for $\epsilon = -3$ as the quantum defect is increased in small steps from $\delta_s = 0$ to $\delta_s = 0.4$, it is possible to witness the growth of core-scattered recurrences (Fig. 11). For $\tilde{S} < 8$, the recurrence spectrum shows little change as the quantum defect is raised, but for $\tilde{S} > 8$, there are conspicuous changes in the recurrence spectrum. The core-scattered recurrences labeled a through f appear and grow monotonically as the quantum defect is increased to $\delta_s = 0.36$, and then they start to decrease.

We can also observe the gradual change of the nearest-neighbor distribution from a Poisson distribution to a Wignerlike distribution for quantum defects between 0 and 0.4. The results are shown in Fig. 12. For $\delta_s = 0.04$ [Fig. 12(a)], the only deviation from the Poisson distribution is a dip in the first bin ($s = 0.05$). As δ_s is increased further, $P(s)$ evolves into a Wigner distribution.
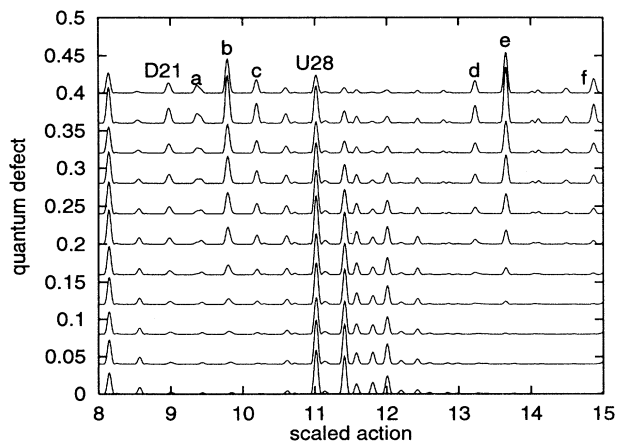

FIG. 11. Evolution of recurrence spectra at $\epsilon = -3$ as the quantum defect δ_s is increased. Features a–f are core-scattered recurrences that appear as δ_s is increased.
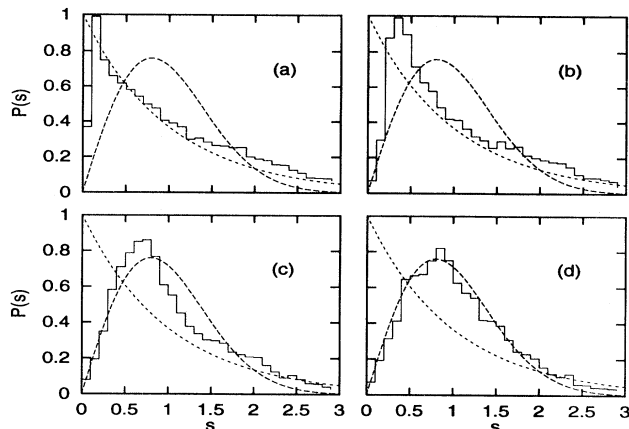

FIG. 12. Nearest-neighbor distributions for increasing value of the quantum defect δ_s for $\epsilon = -2.5$. (a) $\delta_s = 0.04$; (b) $\delta_s = 0.12$; (c) $\delta_s = 0.24$; (d) $\delta_s = 0.32$. Short-dashed line is the Poisson distribution, and the long-dashed line is the Wigner distribution.

3. Core scattering and spectral evolution

In hydrogen, as the scaled energy is decreased, the recurrence spectra display an orderly sequence of bifurcations, as shown in Fig. 13(a). Core scattering in lithium strongly affects the evolution of recurrence spectra as the scaled energy is lowered. To guide the eye, the map is divided into regions A–K. In region A, there are no bifurcations, and most recurrences are small. The variation in the strength of the first peak is probably due to interference between D_1 and U_1. The lowest action sequence of bifurcations is the downhill $n/(n+1)$ sequence and occurs in region B. The uphill $n/(n + 1)$ sequence is adjacent, but at slightly higher action, in region C. These regions begin to overlap near $\epsilon = -4$, and the bifurcation energies of uphill and downhill orbits converge as $\epsilon \rightarrow -\infty$. Region D is a wasteland with no large recurrences. The increase in recurrence strength associated with the downhill $n/(n + 2)$ bifurcations occurs in region E. Region F lies between the downhill and uphill $n/(n + 2)$ bifurcation sequences and has no large recurrences. Region G encloses the large recurrences associated with the uphill sequence of $n/(n+2)$ bifurcations. The increase in recurrence strength associated with the downhill $n/(n + 3)$ bifurcations occurs in region H. Region I is another wasteland between bifurcation sequences, and region J encompasses both the uphill $n/(n + 3)$ and downhill $n/(n + 4)$ bifurcations. Region K is another wasteland.

In lithium, the orderly evolution is strongly affected by core scattering. Figure 13(b) is the corresponding map of computed lithium recurrence spectra. Regions A, B, C, and D at low action are similar to hydrogen. In region E the downhill $n/(n + 2)$ sequence for lithium is generally weaker than for hydrogen. Region F reveals many large recurrences in lithium, though it contains none in hydrogen. Region G has few large recurrences in lithium, whereas in hydrogen it is filled with large re-
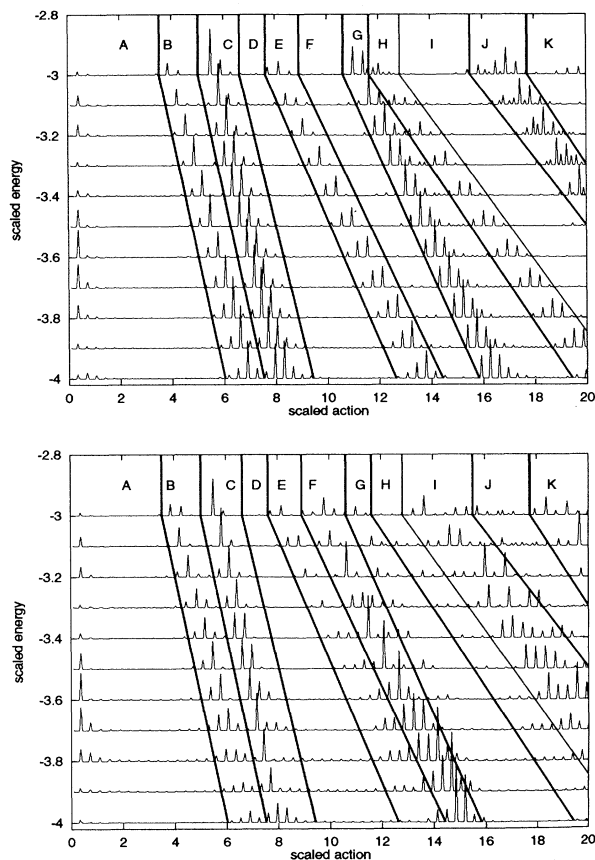
FIG. 13. Computed recurrence spectra for $-4 \leq \epsilon \leq -3$. (a) hydrogen; (b) lithium. Marked regions are discussed in the text.

currences from the uphill $n/(n+2)$ sequence. The explanation is that in hydrogen the large recurrences from the $n/(n+1)$ bifurcation sequences are backscattered, and on their next return, they form the $n/(n+2)$ bifurcation sequences. In lithium, however, the large recurrences from the uphill $n/(n+1)$ bifurcation sequence are scattered into the downhill $n/(n+1)$ bifurcation sequence. When they return a second time, they have actions between the uphill and downhill $n/(n+2)$ sequences. Detailed analysis of the recurrences in region F shows that most of these recurrences are at the action of a large downhill recurrence added to the action of a large uphill recurrence. The dearth of large recurrences in regions G, H, and J, and the plethora in region I can be understood in a similar manner. In summary, the evolution of the recurrence spectrum in lithium is dominated by both bifurcations and core scattering.

4. Recurrence spectra at low scaled energy

To investigate the recurrence spectra at low ϵ, we measured a recurrence spectrum of lithium at $\epsilon = -6$. The constant scaled-energy scan covered roughly $E = -27.9\,\mathrm{cm}^{-1}$ to $E = -37.2\,\mathrm{cm}^{-1}$ while the field was varied from 2.3 V/cm to 4.1 V/cm. This energy range covers

the $n = 54$ to $n = 62$ manifolds, and there is no n mixing in this region.

The experimental recurrence spectrum of lithium is compared with the computed hydrogenic recurrence spectrum in Fig. 14. The first peak at low scaled action corresponds to $\tilde{S}_{cl}(U_1) = 0.286$ and $\tilde{S}_{cl}(D_1) = 0.292$. As the field is reduced to zero, the periods of these orbits converge to the inverse of the zero-field Rydberg separation. The recurrence corresponding to D_1 and U_1 is large because, without n mixing, the Rydberg separation is the strongest frequency in the spectrum. The flurry of peaks at $12 < \tilde{S} < 15$ in the hydrogenic recurrence spectrum is a result of the uphill and downhill $n/(n+1)$ bifurcation sequences, which are also converging. This means that these orbits are destroyed at scaled energies close to where they are created. The period of the newly bifurcated orbits in the $n/(n+1)$ sequence corresponds to the energy spacing between adjacent sublevels of a Stark manifold.

The recurrence spectrum is similar in lithium because before n mixing occurs, the energy levels of lithium and hydrogen follow the same pattern. However, the oscillator strengths are distributed differently, with lithium having most of the oscillator strength in the lowest state in the manifold [20]. Consequently, the recurrences at small multiples of the inverse Rydberg spacing are much stronger in lithium than in hydrogen. Furthermore, the distribution of oscillator strengths among the upper part of the n manifold differs from hydrogen, so the recurrence strengths of the bifurcation peaks at $12 < \tilde{S} < 15$ are also distributed differently.

B. High-action recurrence spectra in the discrete region

We previously reported observation of the signature of very long-period orbits in the Stark spectrum of lithium for $\epsilon = -3$ [11], and for completeness we present some of that data in Fig. 15. We identified recurrences associated with repetitions of the uphill parallel orbit, including those beyond U_{100}. To identify these long-period recurrences, we computed the scaled action by starting and ending the classical orbits near the core radius instead of using the hydrogenic scaled action for the complete tra-
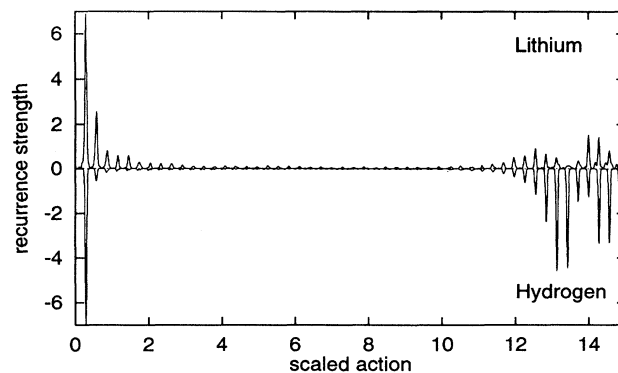

FIG. 14. Recurrence spectra for $\epsilon = -6$. Top: lithium experiment. Bottom: hydrogen computation.
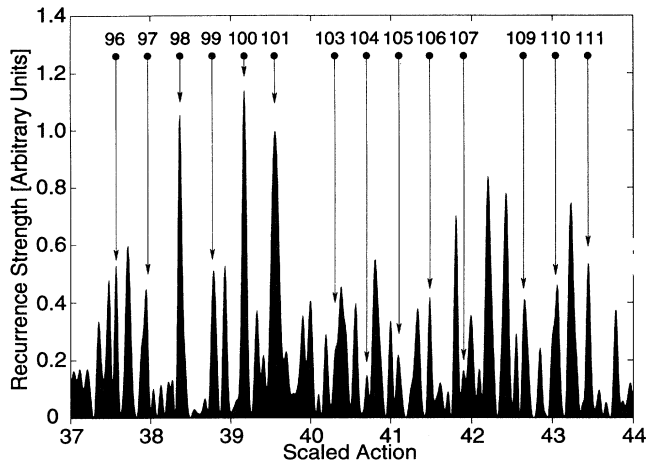
FIG. 15. Experimental recurrence spectrum $\epsilon = -3$. Recurrences identified with repetitions of U_1 are marked with arrows. (From Ref. [11].)

jectory, as described in the Appendix. Consequently, we used $\tilde{S}^{cl}_{Li}(U_1) = 0.3915$ instead of the hydrogenic value, $\tilde{S}^{cl}_H(U_1) = 0.3935$, which is slightly higher. However, we find that the latter produces a small but systematic disagreement with the data that we are unable to explain.

Unlike the case of long-period orbits in the continuum region, we are unable to interpret the downward shift in scaled action as due to the bifurcation shift. For example, the peak identified as U_{101} has a scaled action $\tilde{S}(U_{101}) = 39.56(4)$ that agrees with $101 \times \tilde{S}^{cl}_{Li}(U_1) = 39.54$ but not with $101 \times \tilde{S}^{cl}_H(U_1) = 39.74$. This error cannot be explained by considering the effect of the 94/101 recurrence at $\tilde{S}(94/101) = 39.73$ because its scaled action is too high. The 93/101 orbit at $\tilde{S}(93/101) = 39.63$ is also an unlikely candidate: its scaled action is still too high, and it is likely to have a small recurrence strength at $\epsilon = -3$ because it bifurcated at $\epsilon = -2.72$. This systematic discrepancy remains to be resolved.

IX. SUMMARY AND DISCUSSION

Lithium in an electric field provides an experimentally accessible system for studying the connections between classical and quantum features of a chaotic system. The core induces chaos in the classical system by scattering the valence electron from one hydrogenic trajectory into another each time it passes through the core. For all but the smallest of electric field strengths, this leads to the destruction of tori and ergodic or nearly ergodic motion. In the quantum system, the core-induced chaos is manifest in strong level repulsions and large avoided crossings. The nearest-neighbor distribution of energy levels is in good agreement with the Wigner distribution.

By employing principles of closed-orbit theory, the spectra can be interpreted in terms of classical orbits. Above the classical ionization limit, bifurcations play a dominant role by increasing an orbit's contribution to the spectrum and adding frequency components so that a continuous spectrum can evolve toward a discrete spec-

trum. Below the classical ionization limit, core-scattered ·urrences also have a strong spectral signature. From the point of view of closed-orbit theory, this process accounts for the only difference between lithium and hydrogen. Therefore, it must be the origin of chaos in the quantum system.

Adding the core scattering mechanism to closed-orbit theory may allow computation of the chaotic lithium spectrum using only the hydrogenic orbits. This would circumvent some of the difficulties usually present in the application of closed-orbit theory to chaotic problems. In particular, all of the orbits are stable, and they are easy to compute. However, a general method for including core scattering into closed-orbit theory is lacking, though the work by Dando et al. appears to be a promising step in that direction [23]. An additional complication of core scattering is that multiple core scattering requires including many more terms in the closed-orbit sum and causes an exponential proliferation of recurrences as a function of action, in contrast to the quadratic proliferation of two-dimensional integrable systems such as hydrogen in an electric field.

The possibility of using closed-orbit theory to quantize a chaotic system using the classical mechanics of a related regular system raises the question of whether lithium in an electric field might provide an example of a chaotic system which is approachable by Einstein-Brillouin-Keller tori quantization. Core effects might be included by considering scattering from one hydrogenic torus to another and would cause level repulsions similar to the manner in which tunneling between tori can break energy-level degeneracies.

ACKNOWLEDGMENTS

APPENDIX: SCALED ACTION OF RECURRENCES IN ALKALI-METAL ATOMS

Every peak in a fully resolved recurrence spectrum should occur at the scaled action of a closed orbit. To interpret recurrence spectra of alkali-metal atoms, we need to account for the failure of scaling inside the core region. Two approaches are possible. The first is to use the scaled action of the hydrogenic orbit. The arguments presented below for doing so seem rigorous. The second is to compute the action of an orbit beginning and ending at the core radius, which may seem plausible, but lacks justification. In this case, the orbit only accumulates action in the region of space where the scaling rule holds. Surprisingly, this approach finds some support in the experimental evidence.

In the spectra considered here, the difference between

the two methods is about 0.5% for the scaled action of the uphill and downhill orbits. The difference is hard to detect in the first repetition of a closed orbit, but the difference in the peak position grows linearly with the number of repetitions and becomes noticeable in high-action recurrences.

The total action S of the first repetition of a closed orbit of an alkali-metal Rydberg atom can be written

$$S_{alkali} = S_H + 2\pi\delta_s = 2\pi(w\tilde{S}_H + \delta_s), \qquad (A1)$$

where $\tilde{S}_H$ is the scaled action of a hydrogenic orbit, and δ_s is the s state quantum defect of the alkali metal. From a quantum mechanical viewpoint, Eq. (A1) is obvious because the phase a wave accumulates is simply the classical action, and $2\pi\delta_l$ is the phase shift of the radial wave function. (The slow variation of δ_s with energy can be neglected here.) Consequently, the additional classical action due to the core is $2\pi\delta_s$. In the sum over closed orbits, the quantum defect is a constant phase multiplied by the number of repetitions. However, because it does not depend on the action scaling variable w, it should have no effect on the positions of recurrences.

Equation (A1) has been verified numerically using a model core potential which gives the desired quantum defects. We have computed the actions of closed orbits of the Hamiltonian, which includes the core potential for various values of w. $S(w)$ is a linear function of w. The slope of the line $S(w)$ is $2\pi\tilde{S}$ and the y intercept is $2\pi\delta_s$.

For example, the scaled action of U_1 for $\epsilon = -3$ is $\tilde{S}_H = 0.3935$. The action of this orbit in lithium is

$$S_{Li} = 2\int_0^{z_{max}} \left[2\left(E + \frac{1}{z} - Fz + V_c(z)\right)\right]^{1/2} dz, \qquad (A2)$$

where z_{max} is the classical turning point, and $V_c(z)$ is the core potential reflecting the difference between lithium and hydrogen. S_{Li} is shown as a function of w in Fig. 16 along with the best-fit line. The slope yields $\tilde{S}_{Li} = 0.3935(1)$, and the y intercept yields $\delta_s = 0.426(7)$. A similar computation for the uphill parallel orbit at $\epsilon = -0.4$ gives $\tilde{S}_{Li} = 0.6903(2)$ and $\delta_s = 0.42(1)$. The scaled action for hydrogen is $\tilde{S}_H = 0.6902$. The agreement with
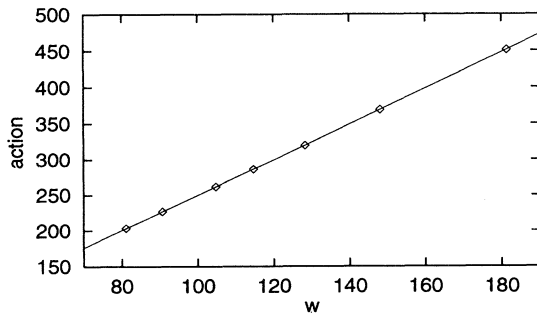
Eq. (A1) is excellent for the scaled actions and good for the quantum defects.

Since the sinusoidal modulation of the spectrum is caused by the part of the action that obeys the scaling rule, peaks in the recurrence spectrum of lithium should be located at the scaled actions of the hydrogenic orbits and their repetitions. This is confirmed by examination of low-action recurrences in experimental and computed recurrence spectra of lithium, and computed recurrence spectra of hydrogen at $\epsilon = -3$, as shown in Table III.

However, before we determined that the scaled action of the hydrogenic orbits should be used, we found good agreement with long-period orbits in the lithium Stark spectrum by using the scaled action of a closed orbit beginning and ending at an estimated core radius [11]. The scaled action of the uphill parallel orbit was taken to be $\tilde{S}_{Li}^{cl}(r_0) = 0.3915$. The recurrence spectrum and peaks corresponding to multiples of this scaled action are shown in Fig. 15.

Some comments should be made concerning the computation of $\tilde{S}_{Li}^{cl}(r_0) = 0.3915$. This number depends on the model core potential. Furthermore, it is not clear whether r_0 should be the root mean square radius or mean radius of the model core potential or of the charge distribution of the ion. Whatever value is taken, some of the charge distribution lies outside of it and thus prevents the scaling rule from being exact. In practice, we obtained $\tilde{S}_{Li}^{cl}(r_0) = 0.3915$ by treating r_0 as an adjustable parameter and finding agreement with long-period experimental recurrences. We found $r_0 = 0.26$, a value between the root mean square of $f(r)$ ($r_{rms} = 0.54$), and the average radius of $f(r)$ ($r_{avg} = 0.21$).

It might appear that treating the core radius as an adjustable parameter effectively makes $\tilde{S}_{Li}^{cl}(r_0)$ an adjustable parameter also. Agreement with some high-action peaks would be easy to achieve by varying $\tilde{S}_{Li}^{cl}(r_0)$. However, by looking at the Fourier transform of the recurrence spectrum, we can show that the dominant frequencies in the recurrence spectrum correspond to $\tilde{S}_{Li}^{cl}(r_0)$ for both the uphill and downhill parallel orbits. This consistency between the uphill and downhill parallel orbits imposes a constraint on the core radius.

To illustrate this constraint, Fig. 17 shows the Fourier transform of the computed lithium recurrence spectrum at $\epsilon = -3$. The peak corresponding to the spacing between repetitions of the uphill orbit corresponds to $\tilde{S}_{Li}^{qm} = 0.3918$. The same peak in the Fourier transform of the experimental lithium recurrence spectrum at $\epsilon = -3$ corresponds to a spacing of $\tilde{S}_{Li}^{exp} = 0.3920(4)$. These

FIG. 16. The action of the primitive uphill orbit, U_1, computed using our model core potential is plotted as a function of w. Diamonds are computed values. Line is given by a least-squares fit whose slope is $2\pi\tilde{S}$ and whose $w = 0$ intercept is roughly $2\pi\delta_s$.

TABLE III. Scaled actions of recurrences in experimental and computed spectra for $\epsilon = -3$.

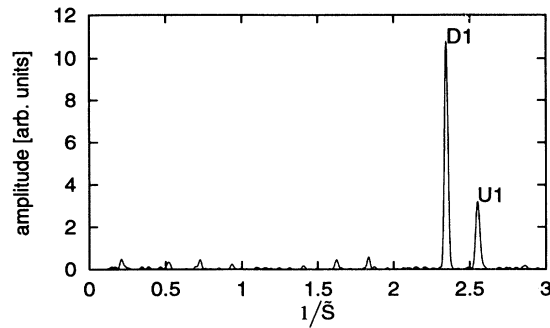| Orbit	$\tilde{S}_H^{cl}$	$\tilde{S}_H^{qm}$	$\tilde{S}_{Li}^{exp}$	$\tilde{S}_{Li}^{qm}$
D_9	3.8600	3.8625	3.8615(39)	3.8627
D_{10}	4.2889	4.2758	4.2784(42)	4.2738
U_{14}	5.5089	5.5084	5.5133(55)	5.5085
U_{15}	5.9024	5.9028	5.9040(59)	5.9034
D_{19}	8.1490	8.1462	8.1396(81)	8.1393

FIG. 17. Fourier transform of the lithium recurrence spectrum at $\epsilon = -3$. The frequencies of the two prominent peaks correspond to the scaled action of U_1 and D_1.

values compare favorably with $\tilde{S}^{cl}_{Li}(r_0) = 0.3915$ for the uphill parallel orbit. The corresponding spacing for hydrogen is $\tilde{S}^{qm}_{H} = 0.3935$, which is in good agreement with $\tilde{S}^{cl}_{H} = 0.3935$ for U_1.

The peak corresponding to the spacing between repetitions of the downhill orbit in the computed lithium recurrence spectra corresponds to $\tilde{S}^{qm}_{Li} = 0.4262$. The same peak in the Fourier transform of the experimental lithium recurrence spectrum at $\epsilon = -3$ corresponds to a spacing of $\tilde{S}^{exp}_{Li} = 0.4260(4)$. These compare favorably with $\tilde{S}^{cl}_{Li}(r_0) = 0.4268$ for D_1. The corresponding spacing for hydrogen is $\tilde{S}^{qm}_{H} = 0.4288$ which is in good

agreement with $\tilde{S}^{cl}_{H} = 0.4289$ for D_1. Consequently, we conclude that the recurrence spectrum has strong underlying periodicities corresponding to $\tilde{S}^{cl}_{Li}(r_0)$ of U_1 and D_1.

We have shown that there are two possible approaches to computing the scaled action of recurrences in spectra of alkali-metal atoms in strong fields. For low action, there appears to be no doubt that the scaled action of recurrences is given by the hydrogenic scaled action. However, for high action it appears that the position of recurrences is given by a scaled action computed by excluding the core region.

We cannot reconcile these seemingly contradictory results, but we mention the possibility of some interference effect causing a frequency pulling. We have tried to account for the shift in the high-action recurrences by some interference effect due to the quantum defect. The closed-orbit sum in Eq. (7) is actually a sum over Fourier series, with each primitive orbit contributing a Fourier series. Replacing S with its value in alkali metals gives

$$Df' = \sum_k \sum_{n=1}^{\infty} D_{nk} \sin\left[2\pi n(w\tilde{S}_H + \delta_s) - \Phi_{nk}\right]. \quad (A3)$$

If the quantum defect were a constant phase in every term, it could not cause a shift in the peak positions. However, the phase due to the quantum defect is multiplied by n, and we are unsure what strange effects this could introduce.

[1] T. F. Gallagher, *Rydberg Atoms* (Cambridge University Press, Cambridge, 1994); *Rydberg States of Atoms and Molecules*, edited by R. F. Stebbings and F. B. Dunning (Cambridge University Press, Cambridge 1983), and references therein; E. Luc-Koenig and A. Bachelier, J. Phys. B **13**, 1769 (1980).

[2] D. Harmin, Phys. Rev. A **26**, 2656 (1982).

[3] F. Haake, *Quantum Signatures of Chaos* (Springer-Verlag, Berlin, 1991).

[4] M. C. Gutzwiller, *Chaos in Classical and Quantum Mechanics* (Springer-Verlag, Berlin, 1990).

[5] M. L. Du and J. B. Delos, Phys. Rev. Lett. **58**, 1731 (1987); Phys. Rev. A **38**, 1896 (1988); **38**, 1913 (1988).

[6] H. Hasegawa, M. Robnik, and G. Wunner, Prog. in Theor. Phys., Suppl. 98, p. 198 (1989), and references therein.

[7] D. Delande and J. C. Gay, Phys. Rev. Lett. **57**, 2006 (1986); D. Wintgen and H. Friedrich, Phys. Rev. Lett. **57**, 571 (1986).

[8] A. Holle, J. Main, G. Wiebusch, H. Rottke, and K. H. Welge, Phys. Rev. Lett. **61**, 161 (1988).

[9] J. Main, G. Wiebusch, K. Welge, J. Shaw, and J. B. Delos, Phys. Rev. A **49**, 847 (1994).

[10] U. Eichmann, K. Richter, D. Wintgen, and W. Sander, Phys. Rev. Lett. **61**, 2438 (1988).

[11] M. Courtney, H. Jiao, N. Spellmeyer, and D. Kleppner, Phys. Rev. Lett. **73**, 1340 (1994).

[12] M. Courtney, H. Jiao, N. Spellmeyer, D. Kleppner, J. Gao, and J. Delos, Phys. Rev. Lett. **74**, 1538 (1995).

[13] J. Gao and J. B. Delos, Phys. Rev. A **49**, 869 (1994).

[14] Peter J. Redmond, Phys. Rev. B **133**, 1352 (1964).

[15] M. Courtney and D. Kleppner, Phys. Rev. A (to be published).

[16] O. Bohigas and M. J. Giannoni, in *Mathematical and Computational Methods in Nuclear Physics*, edited by J. S. DeHessa, J. M. G. Gomez, and A. Polls, Lecture Notes In Physics Vol. 209 (Springer-Verlag, Berlin, 1984).

[17] M. V. Berry and M. Tabor, Proc. R. Soc. London, Ser. A **356**, 375 (1977).

[18] O. Bohigas, M. J. Giannoni, and C. Schmit, Phys. Rev. Lett. **52**, 1 (1984).

[19] For our purposes, the method of Ref. [20] was satisfactory. A more general method is presented by Harmin in Ref. [2].

[20] M. L. Zimmerman, M. G. Littman, M. M. Kash, and D. Kleppner, Phys. Rev. A **20**, 2251 (1979).

[21] J. Gao, J. B. Delos, and M. Baruch, Phys. Rev. A **46**, 1449 (1992); J. Gao and J. B. Delos, *ibid.* **46**, 1455 (1992).

[22] D. Delande, K. T. Taylor, M. H. Halley, T. van der Veldt, W. Vassen, and W. Hogervorst, J. Phys. B **27**, 2771 (1994).

[23] P. A. Dando, T. S. Monteiro, D. Delande, and K. T. Taylor, Phys. Rev. Lett. **74**, 1099 (1995).

[24] T. van der Veldt, W. Vassen, and W. Hogervorst, Europhys. Lett. **21**, 9 (1993).

[25] S. Gerstenkorn and P. Luc, *Atlas of the Absorption Spectra of Molecular Iodine for 14,800 to 20,000 cm^{-1}*, (CNRS, Paris, 1978); S. Gerstenkorn, J. Verges, and J. Chevillard, *Atlas of the Absorption Spectra of Molecular Iodine for 11,000 to 14,000 cm^{-1}*. (CNRS II, Aime Cotton, 1982).

[26] C. Iu, Ph.D. thesis, Massachusetts Institute of Technol-

ogy, 1991.

[27] R. R. Freeman, N. P. Economu, G. C. Bjorkland, and K. T. Lu, Phys. Rev. Lett. **41**, 1463 (1978); R. R. Freeman and N. P. Economu, Phys. Rev. A **20**, 2356 (1979); T. S. Luk, L. DiMauro, T. Bergeman, and H. Metcalf, Phys.

Rev. Lett. **47**, 83 (1981).

[28] M. Kus, F. Haake, and D. Delande, Phys. Rev. Lett. **71**, 2167 (1993).

[29] Note that this recurrence spectrum is from a repeat of the experiment presented in [11] and shown in Fig. 15.